

Enhanced sensitivity deep subwavelength direction-of-arrival sensing using temporal modulation

Tamir Zchut, Yarden Mazor

School Of Electrical Engineering, Tel Aviv University, Tel Aviv, 69978, Israel

February 28, 2023

Abstract

Electromagnetic wave interaction with time-varying systems has gained a lot of research interest in recent years. The temporal modulation gives unprecedented control over the response, allowing us to go beyond the state-of-the-art in passive systems. In this work, we use time variation to derive a model for a deep-subwavelength direction-of-arrival (DoA) sensing apparatus with enhanced performance and sensitivity. We formulate the problem, derive an analytical model, and discuss the various physical mechanisms responsible for the enhancement. We show that time modulation enables a new degree of control that can be used to optimize the response for various incident frequencies, allowing for wideband operation. Additionally, we show that incorporating the currents from higher generated harmonics into the sensing scheme allows us to extract more accurate information about the impinging wave.

1 Introduction

Detecting a wave's direction of arrival (DoA) has important applications in many fields. Starting from the survival of small species in nature, which rely on understanding the direction a predator is approaching based on the sounds it makes, through aviation and radar systems, and even modern-day imaging technologies such as light-field photography. Usually, DoA detectors rely on the phase differences when the EM signal is recorded by two (or more) adjacent elements, bringing forward a significant limitation - what if the difference is very small, as when the sensing apparatus is small compared to the received signal's characteristic wavelength?

Two main approaches exist in electromagnetic (EM) waves to alleviate this limitation. One approach is based on Bio-mimicking small insects. In large animals, significant ear separation lets information regarding the DoA be extracted from the phase/amplitude difference of the recorded sound. In small insects, this problem is mitigated by direct coupling between the ears. This approach is simple to implement and works very well, mainly around a prescribed angle [1]. This was followed up by further optimization, including using high-order modes [2] and non-foster coupling networks [3]. The second approach is using multiphysics systems. One can couple the EM wave response to a different wave mechanism that operates in similar frequencies but significantly smaller wavelengths, which enhances the recorded signal difference. This is demonstrated for an electro-acoustic system in [4].

On a parallel route, in the past decade, EM wave interaction with time-varying systems has seen a burst of renewed interest, driven by two parallel processes. First, the ability to implement such systems has seen significant advances, making the theoretical ideas more realistic. Second, the rise of metamaterials has pointed to many intriguing and exotic wave phenomena occurring in materials with extreme parameters. The basic theoretical concepts are introduced in [5, 6], and numerous applications have been proposed, and among the ones that are more relevant to this work we have the implementation of nonreciprocal elements (gyrators [7], circulators and isolators [8, 9]), Nonreciprocal transmission line design [10], extreme energy accumulation [11], nonreciprocal reflection and transmission [12, 13], and improved antenna matching, Q-factor and bandwidth [14, 15, 16, 17] (many other applications are summarized in [18, 19]). Of specific relevance are the control of Mie scattering properties, shown in [20]. Non-periodic variation and switching also play an important role, demonstrated for broadband matching [21], matched filter design [22], engineered time-reversal spectrum [23], and many more.

In this work, we will examine how we can enhance the sensitivity of DoA detection in deeply subwavelength systems using a different approach - by incorporating temporal modulation to enhance and tailor the physical interactions between the system elements. Since time-modulated systems naturally have many parameters at play, and rich content of physical processes occurring, we will focus on unveiling the physical mechanisms at play that enable sensitivity enhancement.

Several works have already started examining this avenue of time-modulated DoA systems. First, in [24] and subsequent works, periodic switching of the received signal from a DoA sensing dimer is used to enable angle estimation through the ratio of power content in various higher harmonics. However, since only the received signal is switched, physical interaction between the elements does not benefit from these higher harmonics. Moreover, the coupling between the elements, which will be pivotal in this work, does not play a significant role. This makes this strategy viable mostly for $d > \lambda/2$, and not the deeply subwavelength scenario we target. In [25], a time-modulated metasurface was proposed for DoA detection, leveraging the deviations in the diffraction/reflection angles to do the estimation. Again, this work utilizes a system whose size is on the order of λ .

2 Formulation

Naturally, time-modulated wave systems possess many degrees of freedom. On top of the "regular" time-invariant parameters, we also have the modulation frequency, depth, waveform, and the ensuing coupling to higher and lower frequencies. Due to that, the analysis becomes complicated quite rapidly with the addition of components. Since we aim to focus on the physical mechanisms that enhance the DoA sensitivity, we employ a simple model - a 2D dimer. To explore our concept, we use a dimer composed of two infinite wires made of a perfect electric conductor (PEC), as shown in Fig. 1. The incident wave angle θ corresponds to a phase difference of $kd \cos(\theta) \ll 1$. The wires are periodically loaded with $Z_p = Z_s + Z_C$, where Z_s is a static, non-modulated impedance, and Z_C is a time-modulated capacitor $C(t)$. The wires are modeled using their susceptibility α , which determines the induced current $I(\omega)$ (without modulation) on each wire via

$$I(\omega) = \alpha(\omega) E_{tan}^{loc}(\omega), \quad (1)$$

Where $E_{tan}^{loc}(\omega)$ is the tangential component of the local field, which contains both the incident wave, and the field scattered by the other wire, but in the absence of the examined wire itself. For infinite PEC wires, the susceptibility is [26, 27]

$$\alpha^{-1}(\omega) = \alpha_0^{-1}(\omega) + \frac{Z_L}{\Delta}, \quad \alpha_0^{-1}(\omega) = \frac{\eta k}{4} H_0^{(2)}(kr_0) \quad (2)$$

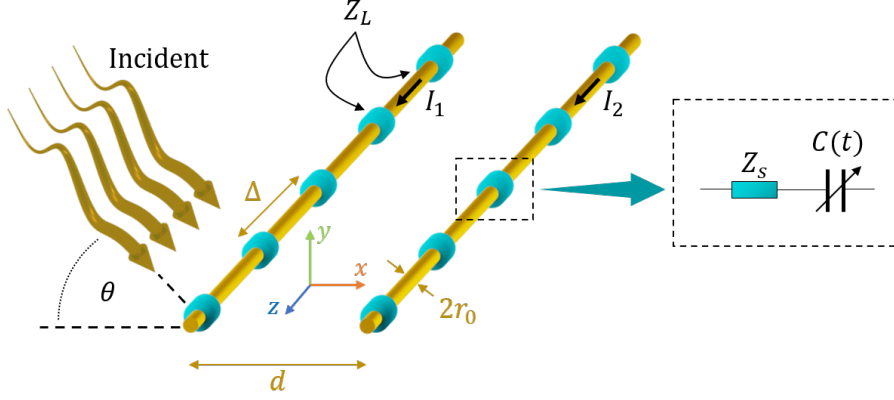


Figure 1: Dimer model: two infinite wires, with periodic loading $Z_L = Z_S + Z_C$, where Z_S is a static impedance, and Z_C is the impedance of a time-modulated capacitor.

Where α_0 is the susceptibility of the unloaded wires, Z_L is the Δ -periodic loading, η is the medium impedance, k is the free-space wavenumber, and $H_0^{(2)}$ is zero-order Hankel function of 2nd kind. To clarify the notation, later we will use also $\gamma = \alpha^{-1}$, $\gamma_0 = \alpha_0^{-1}$, and for simplicity, we focus on TE incidence (therefore \hat{z} electric field). For every frequency ω , the current on the wires generates scattered fields via $E_{tan}^{scattered}(\rho) = G(\rho, \omega)I$, where $G(\rho, \omega)$ is the 2D Green's function of the electric field in free-space, i.e. $G(\rho, \omega) = -\frac{\eta k(\omega)}{4} H_0^{(2)}(k(\omega)\rho)$. Using both G and α , we can express the total reaction of a non-modulated dimer are

$$I_2 = \frac{\alpha_2 E_2^{inc} + G(d)\alpha_1\alpha_2 E_1^{inc}}{1 - G^2(d)\alpha_1\alpha_2}, \quad I_1 = \alpha_1 (E_1^{inc} + G(d)I_2). \quad (3)$$

Now, let us incorporate the effects of periodic temporal modulation into the system. When the capacitor $C(t)$ is periodically modulated, $C(t)^{-1} = C_0^{-1}[1 + m \cos(\omega_m t + \varphi_m)]$, we can represent every physical quantity as a sum of all the possible harmonics

$$X(t) = \sum_{n=-\infty}^{\infty} \tilde{X}_n e^{j(\omega + n\omega_m)t} + c.c. = \sum_{n=-\infty}^{\infty} \tilde{X}_n e^{j\omega_n t} + c.c. \quad (4)$$

Where X can be the current I or the electrical field E or any other relevant quantity, $\omega_n = \omega + n\omega_m$, and c.c. means complex conjugate. Since both the current I and the electric field E_z are excited in multiple frequencies (As expected in our temporally modulated system), the amplitudes of the spectral components can be ordered in a column vector $[\tilde{I}]$, and $[\tilde{E}]$. Using these, and following [6, 26], we can write the time-modulated single wire

response:

$$[\tilde{E}] = \underline{\underline{\mathbf{\Gamma}}}[\tilde{I}] \leftrightarrow \begin{bmatrix} \vdots \\ \tilde{E}_{-1} \\ \tilde{E}_0 \\ \tilde{E}_1 \\ \vdots \end{bmatrix} = \begin{bmatrix} \ddots & \vdots & \vdots & \vdots & 0 \\ \dots & \gamma_0(\omega_{-1}) + \frac{1}{j\omega_{-1}C_0\Delta} & \frac{M}{j\omega_0C_0\Delta} & 0 & \dots \\ \dots & \frac{M^*}{j\omega_{-1}C_0\Delta} & \gamma_0(\omega_0) + \frac{1}{j\omega_0C_0\Delta} & \frac{M}{j\omega_1C_0\Delta} & \dots \\ \dots & 0 & \frac{M^*}{j\omega_0C_0\Delta} & \gamma_0(\omega_1) + \frac{1}{j\omega_1C_0\Delta} & \dots \\ 0 & \vdots & \vdots & \vdots & \ddots \end{bmatrix} \begin{bmatrix} \vdots \\ \tilde{I}_{-1} \\ \tilde{I}_0 \\ \tilde{I}_1 \\ \vdots \end{bmatrix}, \quad (5)$$

Where $M = me^{j\varphi_m}$. Since the current is excited in several frequencies, each of these will generate a scattered field at it's specific frequency. Since G is a function of the frequency ω , it can be formulated using a diagonal matrix, $\underline{\underline{\mathbf{G}}}$

$$\underline{\underline{\mathbf{G}}}(\rho) = \text{diag}[\dots, G(\rho, \omega_{-1}), G(\rho, \omega_0), G(\rho, \omega_1), \dots] \quad (6)$$

Then, for the modulated dimer, the currents can be solved from the following matrix equation

$$\underline{\underline{\mathbf{\Gamma}}}_1[\tilde{I}_1] - \underline{\underline{\mathbf{G}}}[\tilde{I}_2] = [\tilde{E}_1^i], \quad \underline{\underline{\mathbf{\Gamma}}}_2[\tilde{I}_2] - \underline{\underline{\mathbf{G}}}[\tilde{I}_1] = [\tilde{E}_2^i] \quad (7)$$

2.1 Performance metrics

In order to compare the performance and possible benefits of our approach, both with respect to different modulation scenarios and other enhancement schemes, we use the sensitivity S , defined as

$$S(\theta) = \left| 1 - \frac{I_1(\theta)}{I_2(\theta)} \right|^2 \quad (8)$$

which essentially quantifies the relative variation of I_1, I_2 with respect to the incident angle. To accurately extract θ from I_1, I_2 , S should vary with large amplitude against θ .

In addition to the sensitivity, we would also like to define a more simple metric, that will allow us to capture the properties of $S(\theta)$ using a single scalar. This will allow us to characterize the sensitivity curve against various system parameters (wire loading, temporal modulation parameters). To that end, we will use the maximum sensitivity, S_{max} :

$$S_{max} = \max_{\theta} \{S(\theta)\} \quad (9)$$

In the modulated system, S_{max} can be calculated for the different up- and down-converted harmonics (which will prove very beneficial), and therefore we will often use S_{max}^n to indicate

that it was calculated for the n 'th harmonic, where $n = 0$ is the fundamental, incident frequency. S_{max}^{NM} (or any other occurrence of NM) will indicate the non-modulated case.

3 Results and Discussion

3.1 Frequency conversion effects

Various physical mechanisms play a role in enhancing the sensitivity of the dimer response to the DoA. To discuss these systematically, let us start by looking at the S_{max}^n/S_{max}^{NM} vs. the modulation frequency. Figure 2 shows $S_{max}^{\{-1,0,1\}}$ for the following parameters: The radius of the wire is $r_0 = 0.3mm$, the distance between the wires is $d = 5cm$, and the base frequency is $f_0 = 300MHz$. The period of loading is $\Delta = 1cm$, with the load consisting of a periodic resistor $R_L = 0.3m\Omega$, and a capacitance $C^{-1}(t) = C_0^{-1}(1 + m \cos(\omega_m t))$, where $C_0 = 13pF$ and $m = 0.2$. In the fundamental frequency, we see that mostly S^{max} is similar to the non-modulated case (yielding a normalized value close to 1), except for a small region around $\omega_m \approx 2.4\omega$ which exhibits a moderate improvement, $S_{max}^0/S_{max}^{NM} \approx 2.7$. However, when looking at the higher harmonics, we see that the sensitivity becomes much higher at certain values of ω_m ($\omega_m \approx 0.21\omega, 0.42\omega, 2.4\omega$). The effect behind this is composed of the interaction of two mechanisms: the eigenmodes of the dimer and frequency conversion induced by the temporal modulation. In the unmodulated dimer, each wire, incorporated with capacitive loading, is resonant (since the pristine wire response is inductive). When two such resonant wires are placed next to each other to form a dimer, two resonance frequencies exist. Each resonant frequency is characteristic of a specific dimer mode - a symmetric and an anti-symmetric one that form a basis for any current combination that may be excited in the wires. We denote the resonance frequencies of each of these modes $\omega_{sym}, \omega_{anti-sym}$ respectively. How strongly each dimer mode contributes to the total currents is a function of the excitation frequency and the exciting field distribution. Since we want to extract information regarding the DoA from the differences between the currents, we would like to "boost" the content of the anti-symmetric mode as much as possible and how steeply this content varies as a function of the incidence angle (considering that for certain values of θ , namely $\pi/2$ and $3\pi/2$, there is only the symmetric mode, regardless of other parameters,

due to symmetry considerations).

When considering a deep subwavelength dimer, we expect the content of the symmetric mode to be dominant, resulting from the slight difference in exciting field between the dimer wires. This makes the current differences between the wires vary only slightly when changing θ , making it harder to extract information about the DoA.

When adding periodic temporal modulation, another mechanism behind the sensitivity enhancement comes into play - frequency conversion. When the capacitor is allowed to vary with time, we convert the fields in the basic problem to higher (and possibly lower) frequencies, i.e. $\omega_n = \omega_0 + n\omega_m$. When ω_m is chosen such that one of the ω_n frequencies coincides with $\omega_{anti-sym}$ we can obtain a strongly enhanced anti-symmetric mode content in the corresponding n 'th harmonic, which is also steeply dependant on the incident angle θ . This results in a enhanced S_{max}^n for that corresponding harmonic, as seen in figure 2(a,b) for dimer separation $d = 5cm, 1cm$ respectively.

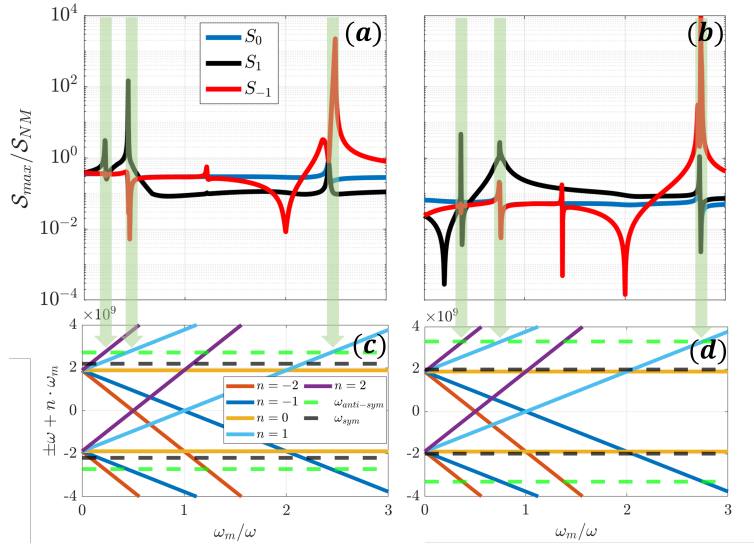


Figure 2: (a) maximum sensitivity as a function of ω_m/ω for harmonics $-1, 0, 1$, and $d = 5cm$ (b) same, for $d = 1cm$ (c) frequency conversion map for $\pm\omega + n \cdot \omega_m$, with $-2 \leq n \leq 2$, and the symmetric and anti-symmetric resonance frequencies. The green arrows indicate connection between peaks in the sensitivity and intersection in the resonance map. (d) Same, for $d = 1cm$.

Using Fig. 2(c,d), we can see the correlation between these two mechanisms, which enhance the sensitivity. The continuous lines represent different ω_n s as a function of ω_m ,

and the dashed lines show the resonance frequency of the symmetric and anti-symmetric modes in the unmodulated dimer. When a continuous line intersects the green dashed line, $\omega_n = \omega_{anti-sym}$ is satisfied for that n'th harmonic, the ω_m values that yield this intersection are roughly the modulation frequencies where we experience a sharp increase in the sensitivity. Thus, by choosing the dimer parameters, we can alter $\omega_{anti-sym}$ and ω_m , and tailor the frequency response we need, to sense the expected θ s better for the required range of operating frequencies. It is essential to add here that while this proves good physical intuition, quantitatively, there are minor deviations in the predicted value of ω_m based on this intuition and the actual value in which the enhancement is most prominent. This is due to the fact that we make use of the resonance frequencies in the *unmodulated system*. These frequencies also experience a shift under modulation since the effective impedance of the wires changes.

Next, we would like to explore additional venues to tune the performance of our dimer. The natural way to do that, is by tailoring the periodic loading Z_L using additional passive elements such as inductors, capacitors, or a combination of the two.

To simplify the calculation we add the components in series. When adding either an inductance L or capacitance C , the load impedance Z_L in the n'th harmonic becomes $Z_L(\omega_n) = R_l + \frac{1}{j\omega_n C_m} + j\omega_n L$ or $Z_C(\omega_n) = R_l + \frac{1}{j\omega_n C_m} + \frac{1}{j\omega_n C}$ respectively. Figure 3 presents the sensitivity dynamics as a function of the values of L, C . In panels (a,b,d,e) we see the sensitivity of both the base harmony S_0 and the first harmony S_1 , as a function of the added passive element (L for (a,d) or C for (b,e)) and of the normalized modulation frequency $\frac{\omega_m}{\omega}$. In all these panels, we see that as the passive element value, L or C , changes, the modulation frequency of the peak ω_m^{peak} changes as well. In these panels, the red line shows the location of the anti-symmetric resonance frequency for the non-modulated circuit, and the yellow lines show the location of the symmetric resonance frequency. As portrayed before, the sensitivity peak modulation frequency moves together with the conversion frequency corresponding to the anti-symmetric mode. These panels show that this concept can be generalized, and the loading can be used to tailor the response to our needs.

When combining inductance and capacitance, we introduce more resonance frequencies into the non-modulated system, which provide additional sensitivity peaks when coinciding

with converted harmonics. For example, when using $Z_L(\omega_n) = R_l + \frac{1}{j\omega_n C_m + \frac{1}{j\omega_n L + \frac{1}{j\omega_n C}}}$ we see in Fig. 3(c,f) how additional peaks for different ω_m values are added to the system, which can be used to design a multi-frequency sensing dimer.

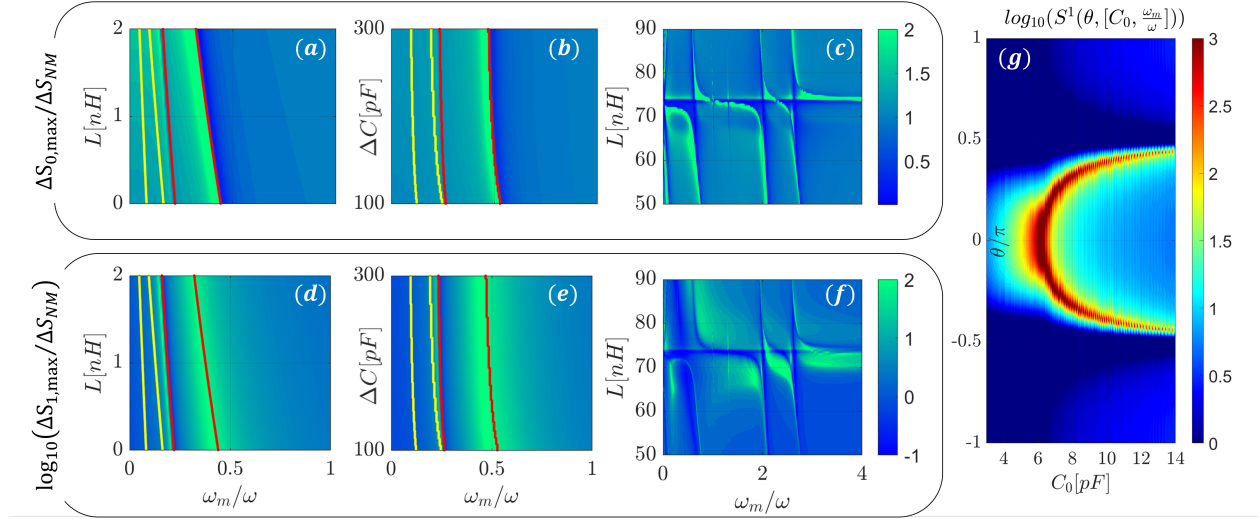


Figure 3: (a,b,c): Normalized maximum sensitivity in the fundamental harmonic, as function of ω_m/ω , and of the value of inductance/capacitance added to Z_L . (d,e,f): Normalized sensitivity of the 1st harmonic, as function of ω_m/ω , and of the value of inductance/capacitance, on a logarithmic scale. The red lines are the evaluated ω_m required for the first harmonic to coincide with the anti-symmetric resonance frequency of the non-modulated circuit (yellow for the symmetric resonance). for (c,f): $C = 3\text{pF}$. (g): $S^1(\theta)$ for varying values of C_0 .

In fig. 3 (g), we see how a change to the modulation capacitor controls the specific θ around which the sensitivity changes most drastically. For each value of C_0 the optimal ω_m is chosen, and S^1 is calculated.

3.2 Energy balance and conversion efficiency

Since our system is time-modulated it is not, in general, passive. Here, we would like to examine the balance between the incident power used to excite the currents P_{inc} and the radiated power P_{rad} to better understand the energy dynamics. Assuming that no material losses are present, the only way energy can exit the system is through radiation. In reality, there are some losses to the wires and the system elements, but the dissipated power is

negligible in comparison with the radiated power. If we define a cylindrical envelope \mathcal{S} with radius $R \rightarrow \infty$, the radiated power given by (Appendix)

$$P_{scat}(\omega) = \frac{\eta^2 k}{4} ([|I_1|^2 + |I_2|^2] + 2J_0(kd)\Re\{I_1 \cdot I_2^*\}) \quad (10)$$

where $J_0(z)$ is 0th order Bessel function. On the other hand, the power extracted from the incident field, $P_{inc}(\omega)$ is given by

$$P_{inc}(\omega) = \frac{1}{2}\Re\{\alpha^*(|\bar{E}_1^{inc}|^2 + \bar{E}_1^{inc}G^*(d)\bar{I}_2^*)\} + \frac{1}{2}\Re\{\alpha^*(|\bar{E}_2^{inc}|^2 + \bar{E}_2^{inc}G^*(d)\bar{I}_1^*)\} \quad (11)$$

When the system is not modulated and lossless, these quantities will be in equilibrium. When time-modulation is introduced, this equilibrium is violated, since the modulation can potentially provide additional power to the system (or act as a sink and extract power). In this case, there are additional frequencies in which current is generated, and therefore power is radiated, rendering the total scattered power as a sum over all possible frequencies

$$P_{scat,tot} = \sum_n P_{scat}(\omega_n).$$

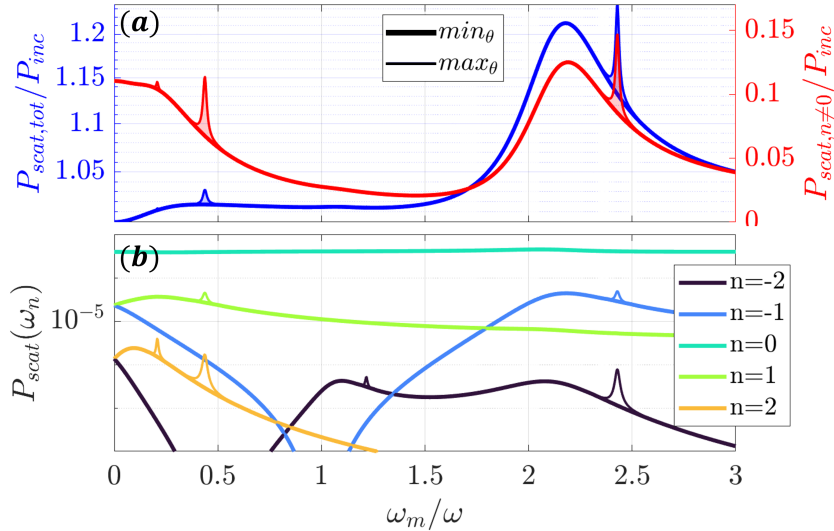


Figure 4: (a) Normalized sum of the total scattered energy (in all harmonics) (blue), and normalized sum of scattered energy in the up- and down-converted harmonics (excluding the fundamental $n = 0$) of the scattered energy (red). (b) scattered energy of 5 harmonics $-2 < n < 2$. Both are functions of the normalized modulation frequency $\frac{\omega_m}{\omega_0}$, and show the difference between the minimal energy as a function of θ (thick line), and the maximum energy as a function of θ (thin line).

In Fig. 4(a), we examine the total power gain (blue) and the up- and down-converted scattered power as a function of the modulation frequency ω_m . For each choice of ω_m the obtained scattered power is also a function of the incidence angle θ , and since we would like to examine these dynamic, we represent each quantity by two different lines: a thick line, which depicts the minimal power as a function of θ , $\min_{\theta}\{P_{scat}\}$, and a thin line, which depicts the maximal energy as a function of θ , $\max_{\theta}\{P_{scat}\}$. Across all examined modulation frequencies a small amount of total gain is provided to the system, since the blue line in 4(a) is always > 1 . Additionally, in certain values of ω_m we see there is a significant difference between the maximum and minimum for different DoA θ . This is a complementary mechanism - when the modulation frequency up- or down-converts to the anti-symmetric dimer mode, the gain provided to the system has a significant variation as a function of θ , playing a role in the resulting enhanced sensitivity to the DoA. Figure 4(b) helps us confirm this picture. We see that the total scattered energy in each harmonic experiences a noticeable dependence on θ (manifesting as a gap between the thick and thin lines) when the conversion corresponds to the anti-symmetric dimer mode. When examining the normalized sum of the converted harmonics (all $n \neq 0$) (red), we see that for modulation frequencies corresponding to conversion to dimer resonances the scattered power is 3 times larger, which indicates the much higher conversion efficiency in this regime.

In fig. 4(a)(red), we notice two types of peaks in sensitivity - peaks for which the amplitude varies as a function of θ (manifesting as a significant gap between maximum and minimum values), and peaks which do not have this "spreading." Another characteristic that is different between these is the width of the peaks. The peaks associated with the anti-symmetric mode are much narrower than the symmetric one. This is due to the fact that the anti-symmetric mode has a significantly higher quality factor (Q factor), a consequence of the fact that the primary "loss" mechanism here is radiation, and the anti-symmetric mode radiates much less efficiently. This can be seen using the scattered energy equation, eq. 10 - for given current magnitude on each wire, when the currents are out of phase ($I_1 = -I_2$) we have $I_1 \cdot I_2^* < 0$, while for the symmetric mode $I_1 \cdot I_2^* > 0$. Since $J_0(kd) \approx 1$, the expected radiated power will be much higher for the symmetric mode than for the anti-symmetric mode.

3.3 Fast modulation

Another possible enhancement mechanism is revealed when examining higher modulation frequencies. While it might be challenging to achieve fast modulations (depending on the incident wave frequency and other system parameters), this physical mechanism exists and may be of use. When examining ΔS_1 for higher values of ω_m , we notice "ripples" that start occurring, when plotting $\Delta S_1(\omega_m/\omega)$, as seen in figure 5(a), in red.

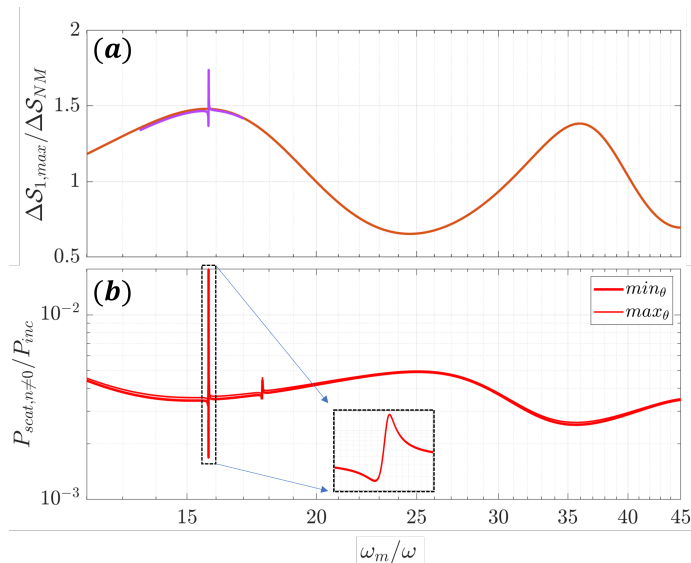


Figure 5: Top: S_{max}^1 as a function of $\frac{\omega_m}{\omega}$, with $10 < \frac{\omega_m}{\omega} < 45$. At $\frac{\omega_m}{\omega} > 20$, we see ripples in the sensitivity. Bottom: normalized energy as function of $\frac{\omega_m}{\omega}$.

This effect happens because the dimer is no longer deep-subwavelength at higher harmonics when the modulation is fast enough. Therefore, the interaction between the wires through the surrounding medium contributes a non-negligible phase difference which causes the exciting field (incident + interaction) to couple better with the antisymmetric dimer mode, enhancing the sensitivity. Since this enhancement is non-resonant, it is milder than we saw previously. However, it can be incorporated with resonance by loading the wires with a resonant impedance in these frequencies, as shown in magenta in figure 5. The basic parameters are the same as in section 3.1, and the additional resonant loading consists of $L_1 \approx 5.24nH, C_1 \approx 0.195pF$ connected similarly to the results shown in Fig. 3(c,f). These are also demonstrated in the scattered power in Fig. 5(b). if we examine the enhance-

ment around $\omega_m \approx 35\omega$ we see no peak in the scattered energy, indicating the non-resonant operation. However, around $\omega_m = 15.7\omega$, we see that the added resonance gives rise to a sharp peak in scattered power in the 1st harmonic, as it significantly increases the conversion efficiency.

3.4 Parametric amplification

Up to now, we have shown several ways the sensitivity benefits from incorporating time modulation. These revolved around the careful design of the dimer resonances, combined with leveraging the frequency conversion processes that occur when applying periodic temporal modulation. In circuits, parametric amplifiers amplify the input voltage by modulating one of the reactive system elements. The most simple case, which we will examine here, is the degenerate regime, where $\omega_m = 2\omega_0$ [28]. Recently, operating in this regime was also shown to enhance small antenna matching performance, and Q-factor [14, 15, 16]. Since the gain in this regime depends on the phase between the incoming signal and the modulation signal, we intuitively expect that this operation mode will both amplify the currents, and enhance the differences between as a function of the DoA, due to differential gain. We start from Eq. 5, 6 and 7. We substitute $\omega_m = 2\omega_0$, and assume, in general, a phase difference of $\delta\phi$ between the modulation and incoming signals. The incident fields, as they should be substituted into Eq. 5 are

$$\begin{aligned} [\tilde{E}_1] &= [\dots, 0, \tilde{E}_0^* e^{-j\delta\phi}, \tilde{E}_0 e^{j\delta\phi}, 0, \dots]^T \\ [\tilde{E}_2] &= [\dots, 0, \tilde{E}_0^* e^{-j\delta\phi + jkd \cos\theta}, \tilde{E}_0 e^{j\delta\phi - jkd \cos\theta}, 0, \dots]^T. \end{aligned} \quad (12)$$

The $\underline{\underline{\mathbf{I}}}$, $\underline{\underline{\mathbf{G}}}$ matrices would have the same structure as described in Eq. 5. Using these to solve the currents in the wires results in current components at all frequencies $\omega = (1 + 2n)\omega_0$. However, since the main interaction we are interested in is the parametric amplification that results from coupling $[-\omega_0, \omega_0]$, we tune the system parameters differently now. We have already established that working at the resonance frequency of the anti-symmetric mode is preferable. In this case, it will have two key effects: first, the baseline sensitivity of the unmodulated dimer will be around the best we can obtain without modulation. Second, the parametric amplification will increase the content of this anti-symmetric mode. And lastly,

operating near a system resonance will greatly simplify the analysis, rendering the currents for $\omega \neq \pm\omega_0$ negligible. Therefore, we use $C_0 \approx 27.2pF$, and truncate $\underline{\underline{\Gamma}}$ and $\underline{\underline{G}}$ into 2×2 matrices, for the main two frequencies in the system $[-\omega_0, \omega_0]$. In addition, we increase the losses to see the effects of parametric amplification more clearly, adding a 2Ω resistance to the periodic loading.

$$\underline{\underline{\Gamma}}_{2 \times 2} = \begin{bmatrix} \gamma_0(-\omega_0) + \frac{1}{-j\omega_0 C_0 \Delta} & \frac{m}{j\omega_0 C_0 \Delta} \\ \frac{m^*}{-j\omega_0 C_0 \Delta} & \gamma_0(\omega_0) + \frac{1}{j\omega_0 C_0 \Delta} \end{bmatrix}, \quad \underline{\underline{G}}_{2 \times 2} = \begin{bmatrix} G(d, -\omega_0) & 0 \\ 0 & G(d, \omega_0) \end{bmatrix} \quad (13)$$

Yielding the wire currents

$$\begin{aligned} [\tilde{I}_2] &= \left[\underline{\underline{\Gamma}}_{2 \times 2} \underline{\underline{G}}_{2 \times 2}^{-1} \underline{\underline{\Gamma}}_{2 \times 2} - \underline{\underline{G}}_{2 \times 2} \right]^{-1} ([\tilde{E}_2] + \underline{\underline{\Gamma}}_{2 \times 2} \underline{\underline{G}}_{2 \times 2}^{-1} [\tilde{E}_1]) \\ [\tilde{I}_1] &= \underline{\underline{\Gamma}}_{2 \times 2}^{-1} ([\tilde{E}_1] + \underline{\underline{G}}_{2 \times 2} [\tilde{I}_2]) \end{aligned} \quad (14)$$

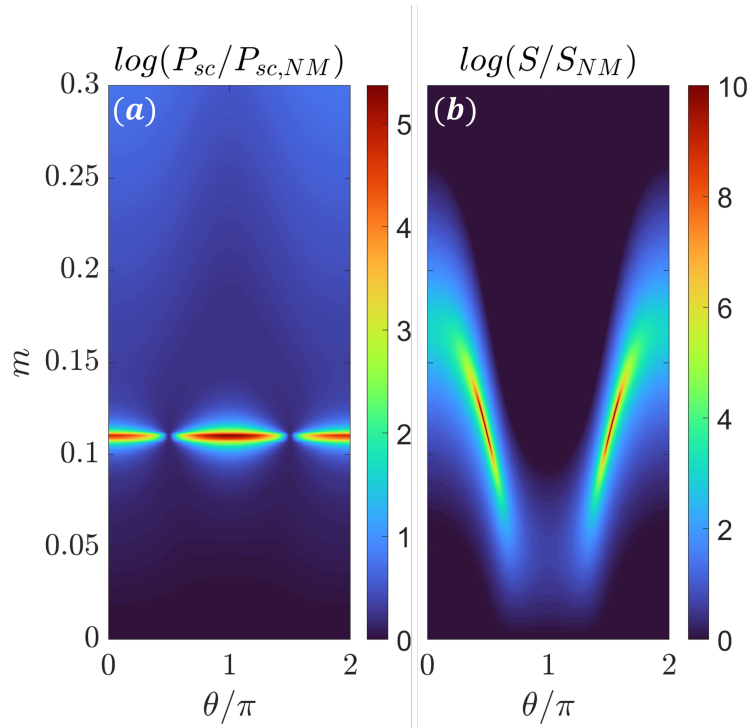


Figure 6: (a) Total scattered power in the PA regime, normalized by the total scattered power of the non-modulated case. Strong amplification occurs only around $m \approx 0.11$. (b) $S(\theta)$, normalized by the sensitivity of the non-modulation case.

In fig. 6(a), the scattered power, normalized by the scattered power of the non-modulated case, is presented as a function of the modulation depth m and of the DoA θ , for $\delta\phi = 0$.

While there is a mild amplification overall, a very strong gain is obtained for a specific value $m \approx 0.11$. This operation regime strongly resembles the negative impedance parametric amplifier [28], so such a strong response around a specific m is expected. Working with this value of m comes along with a sensitive dependence on the choice of other system parameters. However, since the mere amplification of currents is not the sole purpose, we now examine the map of \mathcal{S} . In Fig. 6(b), The normalized sensitivity is presented as a function of m, θ . Here, we see that increased sensitivity can be obtained for a wide range of m values. Moreover, the modulation depth can be used to tune the angle around which the optimal sensitivity is obtained, thus adding a great degree of flexibility that can be controlled by simple means. This shows that while the fundamental operation of the time-modulated system suggested here is similar to a parametric amplifier, the fact that other metrics play a key role is crucial, making this scheme relevant for a much broader range of parameters.

4 Conclusions

In this work, we have focused on studying the physical mechanisms that enhance a deeply-subwavelength dimer's sensitivity to the DoA angle. We have shown that by carefully tuning the modulation parameters, different frequency conversion processes contribute to increased sensitivity. Since the modulation parameters can be tuned, one obtains a highly flexible detector that can be tailored for wide-band operation and enhanced sensing in a specific, varying region of space. Modulating in a parametric amplification regime also contributes to a significant increase in sensitivity and exhibits tunability via the modulation depth and phase.

When designing a DoA detection system, the different effects can be combined. As an example, one can stack two modulation tones, one to convert the incoming signal close to the desired anti-symmetric resonance and one to enhance it parametrically.

Overall, we have shown that the richer physical interactions within the sensing system caused by the temporal modulation can be used to enhance DoA detection in various ways. This study can benefit many applications where the space occupied by the detection system must be extremely small, and many different branches can benefit from this research route.

5 Acknowledgements

Y. Mazor acknowledges support from the Israeli Science Foundation grant 1089/22.

Appendix: Incident and scattered power

Let us assume that for a specific frequency we have the currents I_1, I_2 in the dimer wires.

The far fields generated by the dimer are [29]

$$\begin{aligned} \mathbf{E}_{sc} &= -\frac{\eta k}{4} \sqrt{\frac{2}{\pi k \rho}} \left[I_1 e^{-jk\rho - j\frac{kd \cos(\varphi)}{2} - j\frac{\pi}{4}} + I_2 e^{-jk\rho + j\frac{kd \cos(\varphi)}{2} - j\frac{\pi}{4}} \right] \hat{z} = \\ &= -\frac{\eta k}{4} \sqrt{\frac{2}{\pi k \rho}} e^{-jk\rho - j\frac{\pi}{4}} \left[I_1 e^{-j\frac{kd \cos(\varphi)}{2}} + I_2 e^{j\frac{kd \cos(\varphi)}{2}} \right] \hat{z} \end{aligned} \quad (15)$$

and the corresponding magnetic field is

$$\mathbf{H}_{sc} = \frac{1}{\eta} \hat{\rho} \times \mathbf{E}_{sc} = \frac{1}{\eta} E_{sc} \hat{\varphi}. \quad (16)$$

This yields the scattered power per unit length

$$\begin{aligned} P_{sc} &= \frac{1}{2} \Re \int_0^{2\pi} \mathbf{E}_{sc} \times \mathbf{H}_{sc}^* \rho d\varphi \\ &= \frac{\eta^2 k^2 \rho}{16} \frac{2}{\pi k \rho} |e^{-jk\rho - j\frac{\pi}{4}}|^2 \int_0^{2\pi} d\varphi \left| I_1 e^{-j\frac{kd \cos(\varphi)}{2}} + I_2 e^{j\frac{kd \cos(\varphi)}{2}} \right|^2 \end{aligned} \quad (17)$$

Performing the integration, we get

$$\begin{aligned} P_{sc} &= \frac{\eta^2 k^2 \rho}{16} \frac{2}{\pi k \rho} |e^{-jk\rho - j\frac{\pi}{4}}|^2 \int_0^{2\pi} d\varphi (|I_1|^2 + |I_2|^2) + 2 \Re \{ |I_1| \cdot |I_2| e^{-jk d \cos(\varphi) - \angle(I_1, I_2)} \} \\ &= \frac{\eta^2 k}{4} ([|I_1|^2 + |I_2|^2] + 2J_0(kd) \Re \{ I_1 \cdot I_2^* \}) \end{aligned} \quad (18)$$

Next, P_{inc} is composed of

$$P_{inc} = \frac{1}{2} \Re \{ E_{wire}^{inc} I_{wire}^* \} + \frac{1}{2} \Re \{ E_{other-wire}^{inc} I_{other-wire}^* \} \quad (19)$$

For each wire, the current can be expressed as:

$$I_{wire} = \alpha E_{wire} = \alpha (E^{inc} + G(d) I_{other-wire}) \quad (20)$$

And since the problem is symmetric, we can use it for each wire. Hence:

$$P_{inc} = \frac{1}{2} \Re \{ \alpha^* (|E_1^{inc}|^2 + E_1^{inc} G^*(d) I_2^*) \} + \frac{1}{2} \Re \{ \alpha^* (|E_2^{inc}|^2 + E_2^{inc} G^*(d) I_1^*) \} \quad (21)$$

When modulation is present, we need, in general, to sum up all the contribution from all existing harmonics.

References

- [1] N. Behdad, M. A. Al-Joumayly, and M. Li, “Biologically inspired electrically small antenna arrays with enhanced directional sensitivity,” *IEEE Antennas and Wireless Propagation Letters*, vol. 10, pp. 361–364, 2011.
- [2] S. Yi, M. Zhou, Z. Yu, P. Fan, N. Behdad, D. Lin, K. X. Wang, S. Fan, and M. Brongersma, “Subwavelength angle-sensing photodetectors inspired by directional hearing in small animals,” *Nature nanotechnology*, vol. 13, no. 12, pp. 1143–1147, 2018.
- [3] A. M. Elfrgani and R. G. Rojas, “Biomimetic antenna array using non-foster network to enhance directional sensitivity over broad frequency band,” *IEEE Transactions on Antennas and Propagation*, vol. 64, no. 10, pp. 4297–4305, 2016.
- [4] L. Goltzman and Y. Hadad, “Scattering from artificial piezoelectriclike meta-atoms and molecules,” *Phys. Rev. Lett.*, vol. 120, p. 054301, 2018.
- [5] E. S. Casedy and A. A. Oliner, “Dispersion relations in time-space periodic media: Part i—stable interactions,” *Proceedings of the IEEE*, vol. 51, no. 10, pp. 1342–1359, 1963.
- [6] C. Kurth, “Steady-state analysis of sinusoidal time-variant networks applied to equivalent circuits for transmission networks,” *IEEE Transactions on Circuits and Systems*, vol. 24, no. 11, pp. 610–624, 1977.
- [7] A. K. Kamal, “A parametric device as a nonreciprocal element,” *Proceedings of the IRE*, vol. 48, no. 8, pp. 1424–1430, 1960.
- [8] D. L. Sounas, C. Caloz, and A. Alu, “Giant non-reciprocity at the subwavelength scale using angular momentum-biased metamaterials,” *Nature communications*, vol. 4, no. 1, pp. 1–7, 2013.
- [9] N. A. Estep, D. L. Sounas, J. Soric, and A. Alù, “Magnetic-free non-reciprocity and isolation based on parametrically modulated coupled-resonator loops,” *Nature Physics*, vol. 10, no. 12, pp. 923–927, 2014.

- [10] S. Qin, Q. Xu, and Y. E. Wang, “Nonreciprocal components with distributedly modulated capacitors,” *IEEE Transactions on Microwave Theory and Techniques*, vol. 62, no. 10, pp. 2260–2272, 2014.
- [11] M. Mirmoosa, G. Ptitsyn, V. Asadchy, and S. Tretyakov, “Time-varying reactive elements for extreme accumulation of electromagnetic energy,” *Phys. Rev. Applied*, vol. 11, p. 014024, 2019.
- [12] Y. Hadad, D. L. Sounas, and A. Alu, “Space-time gradient metasurfaces,” *Phys. Rev. B*, vol. 92, p. 100304, 2015.
- [13] Y. Shi, S. Han, and S. Fan, “Optical circulation and isolation based on indirect photonic transitions of guided resonance modes,” *ACS Photonics*, vol. 4, no. 7, pp. 1639–1645, 2017.
- [14] H. Li, A. Mekawy, and A. Alù, “Beyond chu’s limit with floquet impedance matching,” *Phys. Rev. Lett.*, vol. 123, p. 164102, 2019.
- [15] P. Loghmannia and M. Manteghi, “Broadband parametric impedance matching for small antennas using the bode-fano limit: Improving on chu’s limit for loaded small antennas,” *IEEE Antennas and Propagation Magazine*, vol. 64, no. 5, pp. 55–68, 2022.
- [16] A. Mekawy, H. Li, Y. Radi, and A. Alù, “Parametric enhancement of radiation from electrically small antennas,” *Phys. Rev. Appl.*, vol. 15, p. 054063, May 2021.
- [17] A. Shlivinski and Y. Hadad, “Indirect time-modulation of antennas: a venue beyond size dependent bounds,” *arXiv.org*, no. 2209.04841, 2022.
- [18] C. Caloz and Z. Deck-Léger, “Spacetime metamaterials—part ii: Theory and applications,” *IEEE Transactions on Antennas and Propagation*, vol. 68, no. 3, pp. 1583–1598, 2020.
- [19] A. Kord, D. L. Sounas, and A. Alù, “Microwave nonreciprocity,” *Proceedings of the IEEE*, vol. 108, no. 10, pp. 1728–1758, 2020.

- [20] V. Asadchy, A. Lamprianidis, G. Ptitsyn, M. Albooyeh, Rituraj, T. Karamanos, R. Alaei, S. Tretyakov, C. Rockstuhl, and S. Fan, “Parametric mie resonances and directional amplification in time-modulated scatterers,” *Phys. Rev. Appl.*, vol. 18, p. 054065, Nov 2022.
- [21] A. Shlivinski and Y. Hadad, “Beyond the bode-fano bound: Wideband impedance matching for short pulses using temporal switching of transmission-line parameters,” *Phys. Rev. Lett.*, vol. 121, p. 204301, 2018.
- [22] O. Silbiger and Y. Hadad, “Optimization-free filter and matched-filter design through spatial and temporal soft switching of the dielectric constant,” *Phys. Rev. Appl.*, vol. 19, p. 014047, Jan 2023.
- [23] E. Galiffi, S. Yin, and A. Alú, “Tapered photonic switching,” *Nanophotonics*, vol. 11, no. 16, pp. 3575–3581, 2022.
- [24] C. He, X. Liang, Z. Li, J. Geng, and R. Jin, “Direction finding by time-modulated array with harmonic characteristic analysis,” *IEEE Antennas and Wireless Propagation Letters*, vol. 14, pp. 642–645, 2015.
- [25] X. Fang, M. Li, J. Han, D. Ramaccia, A. Toscano, F. Bilotti, and D. Ding, “Accurate direction-of-arrival estimation method based on space-time modulated metasurface,” *IEEE Transactions on Antennas and Propagation*, vol. 70, no. 11, pp. 10951–10964, 2022.
- [26] Y. Hadad and D. Sounas, “Space-time modulated loaded-wire metagratings for magnetless nonreciprocity and near-complete frequency conversion,” *arXiv.org*, no. 1906.00215, 2019.
- [27] S. Tretyakov, *Analytical modeling in applied electromagnetics*. Artech House, 2003.
- [28] R. Collin, *Foundations for microwave engineering*. 1992.
- [29] R. Harrington, “Time-harmonic electromagnetic fields/harrington rf-new-york, chichester,” 2001.